Exploring the edge

Contigiani, O.

Chapter 2

Weak-lensing constraints on splashback around massive clusters

The splashback radius $r_{\rm sp}$ separates the physical regimes of collapsed and infalling material around massive dark matter halos. In cosmological simulations, this location is associated with a steepening of the spherically averaged density profile $\rho(r)$. In this work, we measure the splashback feature in the stacked weak gravitational lensing signal of 27 massive clusters from the Cluster Canadian Comparison Project with careful control of residual systematics effects. We find that the shear introduced by the presence of additional structure along the line of sight significantly affects the noise at large clustercentric distances. Although we do not detect a significant steepening, the use of a simple parametric model enables us to measure both $r_{\rm sp} = 3.5^{+1.1}_{-0.7}$ comoving Mpc and the value of the logarithmic slope $\gamma = \log \rho / \log r$ at this point, $\gamma(r_{\rm sp}) = -4.3^{+1.0}_{-1.5}$.

Omar Contigiani, Henk Hoekstra, and Yannick Bahé
2019, Monthly Notices of the Royal Astronomical Society, 485, 408

2.1 Introduction

In the concordance lambda cold dark matter (ΛCDM) model, collisionless dark matter acts as the building block of cosmic structure, contributing about 25 percent of the total energy density in the Universe and the majority of the total mass (Planck Collaboration, 2016). In this framework, gravity is the primary force behind the growth of structure in the matter field and is able to form the present-day cosmic web from an almost homogeneous initial state. Fully collapsed structures, known as halos, are thought to grow both through mergers of smaller ones (hierarchical clustering) and continuous infall of ambient dark matter (smooth accretion).

An intuitive understanding of this second mechanism is given by the study of spherical collapse in an expanding Universe (see Gunn and Gott, 1972; Fillmore and Goldreich, 1984, for some historic landmark results). Shells of material surrounding an overdensity eventually decouple from the Hubble flow and start collapsing toward it. As more shells orbit the halo, the wrapping in phase space of different streams results in caustics visible in the density profile. Of particular interest is the region around the outermost caustic, where the physical regimes of accreting and collapsed material meet.

More recently, Diemer and Kravtsov (2014, DK14 from now on) studied the spherically averaged density profile $\rho(r)$ of these regions in dark matter only simulations and have reported a change in slope compared to the collisionless equilibrium profile (Einasto or NFW, Einasto, 1965; Navarro et al., 1997). More et al. (2015) argued that the splashback radius $r_{\rm sp}$, corresponding to the minimum logarithmic slope $\gamma(r) = \log \rho(r) / \log r$, could function as a physically motivated definition for the boundary of dark matter halos. This role is usually assumed by proxies for the virial radius such as r_{200m}, defined as the radius inside which the average halo density is 200 times the average matter density of the Universe ρ_m. While this radius has a clear definition based on analytical solutions of idealized virialization scenarios, the mass contained within it, known as M_{200m}, is an imperfect measure of the halo mass. This is because it is subject to a pseudo-evolution caused by the redshift dependence of ρ_m (Diemer et al., 2013). In contrast, because the caustic associated with splashback is connected to the apocenter of recently accreted material, all the material within $r_{\rm sp}$ is necessarily collapsed material and should rightfully contribute to the halo mass.

At larger distances, the presence of correlated structure surrounding the halo is expected to shape the density profile. Using the language of the halo model (see e.g. Cooray and Sheth, 2002, for a review), this is a transition region from the 1-halo term to the 2-halo term. DK14 have however reported that in the outermost regions ($r \lesssim 9r_{200m}$), the 2-halo term based on the matter correlation function provides a worse fit to simulations compared to a simple power law.

Because the slope of the density profile at $r_{\rm sp}$ is found to be, on average, a decreasing function of the halo mass, DK14 first pointed out that large overdensities are the

ideal target for the detection of this feature – i.e. measuring a significant departure from the equilibrium profile. This makes galaxy clusters the ideal candidates since they correspond to the most massive halos in the Universe. For this mass range, $r_{\rm sp}$ is expected to be located around r_{200m}, at a cluster-centric distance of the order of a few Mpc.

The splashback feature should also be present in the radial distribution of galaxies. This was first detected by More et al. (2016) using the large sample of redMaPPer clusters from Rykoff et al. (2014), and studied further in Baxter et al. (2017). However, these studies find a discrepancy between the inferred splashback radius and the expected distribution of subhalos based on dark matter only simulations. Known physical processes (e.g. tidal disruption and dynamical friction) are not expected to induce a mismatch between the galaxy and subhalo distributions at splashback scales and this deviation is still unexplained. In particular, while the results have been shown to depend on the details of the cluster finding algorithm (Zu et al., 2017; Busch and White, 2017), it is still uncertain if this can fully explain the discrepancy (Chang et al., 2018).

Chang et al. (2018) studied a sample of redMaPPer clusters selected in Dark Energy Survey year 1 data. For this large sample, they detected a splashback feature in the galaxy distribution *and* from weak lensing measurements. The latter has the advantage that the lensing signal probes the matter distribution directly (see e.g. Hoekstra et al., 2013, for a review). The first attempt to detect the splashback feature using weak gravitational lensing was presented in Umetsu and Diemer (2017), who used a sample of 16 high-mass clusters in the Cluster Lensing and Supernova survey with Hubble (CLASH). Unfortunately, the limited field of view (foV) of Suprime-Cam prevented precise measurements in the outer regions, and as a result, Umetsu and Diemer (2017) could only provide a lower limit on the splashback radius.

In this work, we provide a measurement[1] of splashback using weak lensing observations for a sample of 27 massive clusters of galaxies that were observed as part of the Canadian Cluster Comparison Project (CCCP; Hoekstra et al., 2012). Hence our strategy is similar to that employed by Umetsu and Diemer (2017), but we take advantage of the fact that the CCCP observations were obtained using MegaCam, which has a foV of 1 deg^2, and enables us to measure the lensing signal beyond the splashback radius. The chaper is organized as follows: in Sec. 2.2 we present our dataset and describe our lensing analysis, in Sec. 2.3 we show the results of our fit and the implications for splashback, and in Sec. 2.4 we draw our conclusions. Throughout the chapter we employ a flat ΛCDM cosmology with $H_0 = 70\,\mathrm{km\ s^{-1}\ Mpc^{-1}}$, $\Omega_m = 0.3$, $\Omega_c = 0.25$ and $\sigma_8 = 0.80$.

[1]In the interest of reproducibility we make our splashback code publicly available at https://github.com/contigiani/splash/.

Table 2.1: The full cluster sample, 'CCCP all', used in this chapter. RA and Dec. are the sky position of the cluster center (brightest cluster galaxy, or X-ray peak for coordinates marked with §), z is the cluster redshift, $\langle\beta\rangle$ is the average value of $D_{\rm LS}/D_{\rm S}$ (see Sec. 2.2.2), M_g is the gas mass within r_{500c}, defined as the radius of the sphere inside which the mean halo density is 500 times the critical density of the Universe at redshift z and M_{200m} is the mass enclosed within r_{200m}. These values are recovered from the NFW fit performed in H15. The values for M_g are taken from the X-ray analysis of M13 or, for values marked with †, they are defined using the scaling relations found in the same paper. Clusters listed below the horizontal line belong to the high-mass subsample.

Name	RA (J2000)	Dec. (J2000)	z	$\langle\beta\rangle$	$M_{\rm g}$ [10^{13} M$_\odot$]	M$_{\rm 200m}$ [10^{14} M$_\odot$]
MS 0440.5+0204	$04^{\rm h}43^{\rm m}09.0^{\rm s}$	$+02°10'19''$	0.19	0.656	2.4	3.8
Abell 1234	$11^{\rm h}22^{\rm m}30.0^{\rm s}$	$+21°24'22''$	0.163	0.699	3.8†	8.3
RX J1524.6+0957	$15^{\rm h}24^{\rm m}38.3^{\rm s}$	$+09°57'43''$	0.516	0.329	4.1	6.5
Abell 1942	$14^{\rm h}38^{\rm m}21.9^{\rm s}$	$+03°40'13''$	0.224	0.621	4.4	14.6
Abell 2259	$17^{\rm h}20^{\rm m}09.7^{\rm s}$	$+27°40'08''$	0.164	0.697	5.0	8.6
MACS J0913.7+4056	$09^{\rm h}13^{\rm m}45.5^{\rm s}$	$+40°56'29''$	0.442	0.396	5.3	6.8
Abell 1246	$11^{\rm h}23^{\rm m}58.5^{\rm s}$	$+21°28'50''$	0.19	0.661	5.6†	9.5
MS 1008.1-1224	$10^{\rm h}10^{\rm m}32.3^{\rm s}$	$-12°39'53''$	0.301	0.526	5.8	17.4
3C295	$14^{\rm h}11^{\rm m}20.6^{\rm s}$	$+52°12'10''$	0.46	0.374	6.2	12.6
Abell 586	$07^{\rm h}32^{\rm m}20.3^{\rm s}$	$+31°38'01''$	0.171	0.674	6.5	5.0
Abell 611	$08^{\rm h}00^{\rm m}56.8^{\rm s}$	$+36°03'24''$	0.288	0.533	6.6	10.0
Abell 2104	$15^{\rm h}40^{\rm m}07.9^{\rm s}$	$-03°18'16''$	0.153	0.712	6.8	17.2
Abell 2111	$15^{\rm h}39^{\rm m}40.5^{\rm s}$	$+34°25'40.5''$	0.229	0.614	7.4	10.2
Abell 959	$10^{\rm h}17^{\rm m}36.0^{\rm s}$	$+59°34'02''$	0.286	0.549	7.5	21.1
Abell 520	$04^{\rm h}54^{\rm m}10.1^{\rm s\S\S}$	$+02°55'18''^{\S}$	0.199	0.654	8.5	16.6

Abell 2537	$23^{\mathrm{h}}08^{\mathrm{m}}22.2^{\mathrm{s}}$	$-02°11'32''$	0.295	0.532	8.6	22.4
Abell 851	$09^{\mathrm{h}}42^{\mathrm{m}}57.5^{\mathrm{s}\S}$	$+46°58'50''^{\S}$	0.407	0.421	9.7	22.6
Abell 1914	$14^{\mathrm{h}}26^{\mathrm{m}}02.8^{\mathrm{s}\S}$	$+37°49'28''^{\S}$	0.171	0.693	9.9	14.7
MS 0451.6-0305	$04^{\mathrm{h}}54^{\mathrm{m}}10.8^{\mathrm{s}}$	$-03°00'51''$	0.54	0.315	10.3	18.0
Abell 521	$04^{\mathrm{h}}54^{\mathrm{m}}06.9^{\mathrm{s}}$	$-10°13'25''$	0.253	0.577	10.6	11.5
Abell 2204	$16^{\mathrm{h}}32^{\mathrm{m}}47.0^{\mathrm{s}}$	$+05°34'33''$	0.152	0.714	11.6	21.8
Abell 1835	$14^{\mathrm{h}}01^{\mathrm{m}}02.1^{\mathrm{s}}$	$+02°52'43''$	0.253	0.58	12.1	21.5
Abell 2261	$17^{\mathrm{h}}22^{\mathrm{m}}27.2^{\mathrm{s}}$	$+32°07'58''$	0.224	0.621	14.6	26.4
CIZA J1938+54	$19^{\mathrm{h}}38^{\mathrm{m}}18.1^{\mathrm{s}}$	$+54°09'40''$	0.26	0.569	$15.6^{\dagger}$	18.6
Abell 697	$08^{\mathrm{h}}42^{\mathrm{m}}57.6^{\mathrm{s}}$	$+36°21'59''$	0.282	0.552	15.6	15.1
RX J1347.5-1145	$13^{\mathrm{h}}47^{\mathrm{m}}30.1^{\mathrm{s}}$	$-11°45'09''$	0.451	0.377	16.3	20.9
Abell 2163	$16^{\mathrm{h}}15^{\mathrm{m}}49.0^{\mathrm{s}}$	$-06°08'41''$	0.203	0.63	23.3	18.9

2.2 Cluster lensing

In this section, we discuss how the sheared images of distant galaxies can be used to constrain the matter distribution of clusters along the line of sight. After introducing our cluster sample, we present the weak lensing measurements and explain our methodology, with a particular focus on systematic effects and noise estimation.

2.2.1 Sample characterization

Our dataset is based on CCCP, a survey targeting X-ray selected massive clusters at $z \lesssim 0.5$ introduced for the first time in Hoekstra et al. (2012) and re-analyzed in Hoekstra et al. (2015, H15 from now on). The starting points of our analysis are the r-band images of 27 clusters captured by MegaCam at the Canada–France–Hawaii Telescope (CHFT). We exclude from the original CCCP images those corresponding to ongoing mergers: Abell 115, Abell 222/3, Abell 1758, and MACS J0717.5+3745 because these systems display a visible double peaked matter distribution for which two splashback surfaces might intersect each other.

The objects are characterized by masses $3.8 < M_{200m}/(10^{14}\ \mathrm{M}_\odot) < 26.4$ and cover a redshift range $0.15 < z < 0.55$, with only six of them located at $z > 0.3$. Table 2.1 reviews the sample and presents the quantities relevant for this work. For more details about the cluster sample we refer the reader to Hoekstra et al. (2012), H15 for a description of the weak lensing analysis, and the companion paper Mahdavi et al. (2013) for the analysis of X-ray observations.

In simulations, DK14 found a correlation between the splashback feature and the halo mass. We, therefore, define a high-mass subsample of our clusters, containing the 13 most massive objects. The average M_{200m} of the sample and the subsample, weighted by the signal-to-noise ratio (SNR), equal 1.7 and $2.0 \times 10^{15}\ \mathrm{M}_\odot$, respectively. We choose to employ the gas mass M_g within r_{500c} reported by Mahdavi et al. (2013) to define our high-mass threshold. This is because this value is found to be a robust estimator of the weak lensing mass and its measurement is mostly independent of it since it is based on a different physical mechanism. A weak dependence between the two is left due to the lensing-based definition of r_{500c}.

Targeted observations such as the ones discussed in this work currently represent the most efficient approach to study clusters of virial mass around $10^{15}\ \mathrm{M}_\odot$. In particular, such a sample cannot be obtained by present-day or near-future wide surveys, e.g. DES (DES Collaboration, 2017) or the Kilo-Degree Survey (KiDS collaboration, 2017), because massive halos are rare (i.e. $\ll 1$ per FoV) and targeted deep data result in a higher SNR compared to wide surveys. For these reasons, the SDSS and DES studies of More et al. (2016), Baxter et al. (2017) and Chang et al. (2018) are based instead on large samples of low-mass clusters: 8649 clusters with $\langle M_{200m} \rangle = 2.7 \times 10^{14}\ \mathrm{M}_\odot$ for SDSS (Miyatake et al., 2016) and 3684 clusters with $\langle M_{200m} \rangle = 3.6 \times 10^{14}\ \mathrm{M}_\odot$ for DES Y1. In contrast, our dataset is much closer in nature to the CLASH sample used in Umetsu

and Diemer (2017), also based on targeted observations. In particular, the mass of their stacked ensemble, $M_{200m} = 1.9 \times 10^{15}$ $M_\odot$, matches ours. Nevertheless, we want to mention one feature unique to CCCP: the FoV of MegaCam (1×1 deg) is significantly larger than that of Suprime-Cam (34×27 arcmin), the instrument used for the CLASH profile reconstruction at large scales (Umetsu et al., 2016). This is particularly suited for our purposes since it allows us to better cover cluster-centric distances where the splashback radius is located.

2.2.2 Tangential shear

In the weak lensing regime, the shear field is found by averaging the PSF-corrected ellipticities of a sample of background sources. We follow H15 and use sources in the magnitude range $22 < m_r < 25$. The lower limit reduces the presence of foreground objects such as bright galaxies belonging to the clusters, which are abundant in the central regions and are not sheared by the cluster's mass distribution. Because this operation is unable to completely remove cluster members, we chose to model the residual contamination statistically, as explained in Sec. 2.2.3.

Shapes are measured using an improved KSB method (Kaiser et al., 1995; Luppino and Kaiser, 1997; Hoekstra et al., 1998). The quadrupole moments of the galaxy images are used to construct a polarization tensor e, which is then corrected for the point spread function (PSF) of the observing instrument. In Sec. 2.2.3 we address this step in more detail and mention the improvements we have implemented since H15. The shear polarizability $\tilde{P}^\gamma$ quantifies how the observed polarization of an individual galaxy is related to the gravitational shear. For an ensemble of sources the shear components are hence measured as a noise-weighted average, $\langle e_i/\tilde{P}^\gamma \rangle$, where the individual weights are written as (Hoekstra et al., 2000)

$$w = \frac{1}{\langle \epsilon^2 \rangle + \left(\sigma_e/\tilde{P}^\gamma\right)^2}. \tag{2.1}$$

In this expression two sources of noise are included: the scatter introduced by the intrinsic variance of galaxy ellipticities $\langle \epsilon^2 \rangle$ and the uncertainty in the measured polarization σ_e due to noise in the imaging data. Following Hoekstra et al. (2000) we use $\langle \epsilon^2 \rangle^{1/2} = 0.25$.

For an isolated circular overdensity, the induced shear is purely tangential, i.e. the deformation is parallel to the radial direction. In general, this shear component is related to the projected mass surface density $\Sigma(R)$ as a function of the radial coordinate

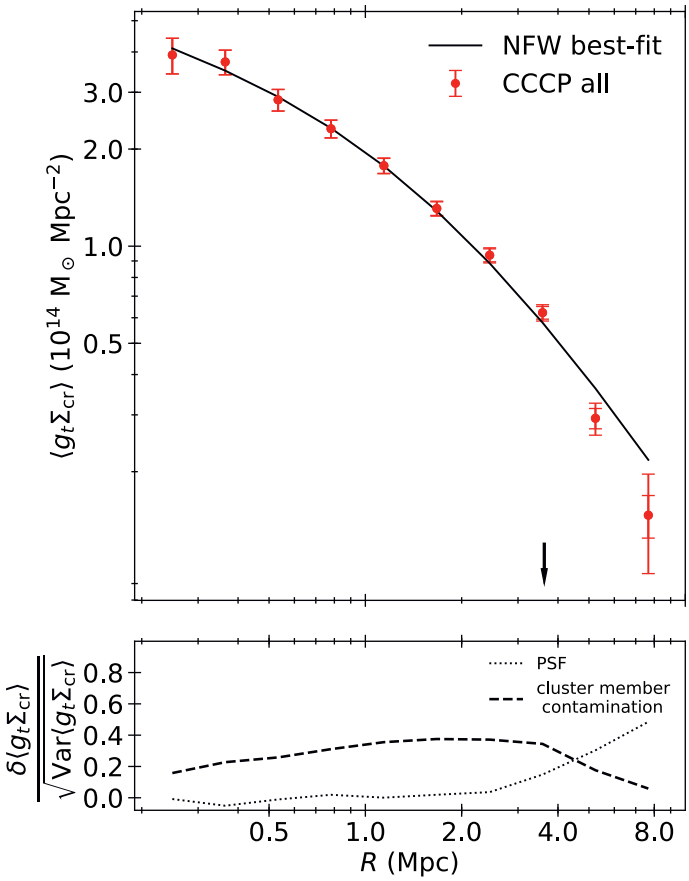

Figure 2.1: Lensing signal. The top panel shows the noise-weighted stacked signal of the 27 clusters in our sample as a function of comoving clustercentric distance, together with a best-fitting NFW profile to the first five data points (see Sec. 2.2.2 for more information). The arrow points to the inferred location of r_{200m}; in simulated galaxy clusters the splashback feature is located around this position. The larger error bars are the full 1σ errors for the data points, while the inner error bars account only for statistical uncertainty. The difference between the two is apparent only in the last few data points. The bottom panel shows an estimate of the expected residual systematics left after the corrections discussed in Sec. 2.2.3 are applied, expressed as a fraction of the total uncertainty. These effects are found to be consistent with the error bars.

R:

$$\gamma_{\rm t}(R) = \frac{\overline{\Sigma}(< R) - \Sigma(R)}{\Sigma_{\rm cr}} = \frac{\Delta\Sigma(R)}{\Sigma_{\rm cr}}, \tag{2.2}$$

$$\Sigma_{\rm cr} = \frac{c^2}{4\pi G}\frac{1}{\langle\beta\rangle}\frac{1}{D_{\rm L}}. \tag{2.3}$$

In these expressions, the profile $\Delta\Sigma(R)$ is called excess surface density and the critical density $\Sigma_{\rm cr}$ is a geometrical factor quantifying the lensing efficiency as a function of the relative position of source and lens. The definition above applies for a lens at distance $D_{\rm L}$ shearing an ensemble of sources. $\langle\beta\rangle$ is the average of the quantity max $[0, D_{\rm LS}/D_{\rm S}]$ for each source, with $D_{\rm LS}$ being the individual lens-to-source distance[2] and $D_{\rm S}$ the distance to the source.

Because we work with single-band observations, we are unable to derive individual photometric redshifts. Fortunately, a representative photometric redshift distribution is sufficient to estimate β. This distribution is obtained for all clusters by magnitude-matching the most recent COSMOS photometric catalog (COSMOS2015, Laigle et al., 2016) to our source r-band magnitude range.

We point out that the measured average ellipticity is an estimator of the reduced shear

$$g_i = \frac{\gamma_i(R)}{1 - \Sigma(R)/\Sigma_{\rm crit}}. \tag{2.4}$$

However, because we are interested in constraining a feature located in a low-density region, for our main analysis we will assume the first-order approximation $g_i \simeq \gamma_i$ when fitting a model. From our source catalogs we extract the tangential component $g_{\rm t}(\theta_j)$ in radial bins and estimate for each cluster the data covariance matrix as the sum of two terms: the first accounts for statistical noise in the average ellipticity and the second one takes into account the presence of additional shear introduced by uncorrelated structure along the line of sight. More details about the evaluation are presented in Appendix 2A.

The top panel of Figure 2.1 presents the average noise-weighted signal of the full cluster sample. The double error bars in the figure illustrate how the inclusion of the second source of noise has an impact on the uncertainties at large scales. An indicative NFW fit, obtained using the virial overdensity from Bryan and Norman (1998) at an assumed redshift $z = 0.25$, is also shown. The position of r_{200m} for the best-fit model is also indicated in the same figure.

[2]Note that $D_{\rm LS}$ is negative for foreground sources.

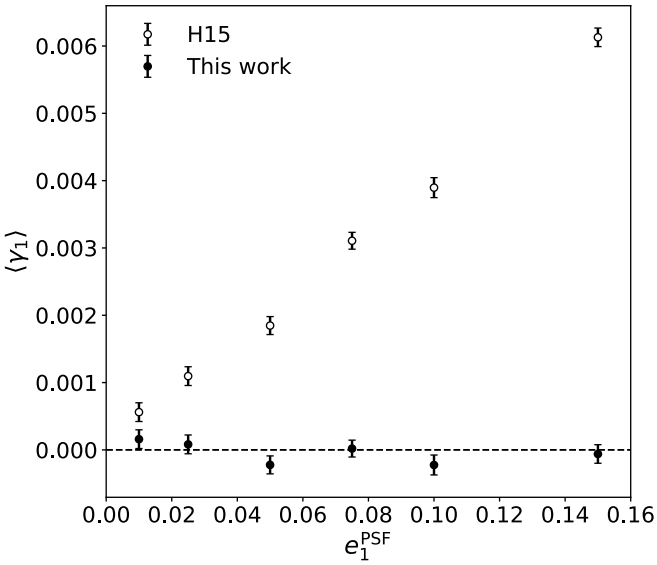

Figure 2.2: PSF correction improvements. Image simulations are used to quantify the residual additive bias not captured by the correction obtained in H15. The circles show how residual additive bias in the average shear $\langle \gamma_1 \rangle$ was present in the presence of simulated PSF anisotropy ($e_1^{\rm PSF} \neq 0$). In this work (filled points) we are able to nullify this effect by boosting the KSB smear polarizability $P^{\rm sm}$. See Sec. 2.2.3 for more details.

2.2.3 Residual systematics

In this section, we address the effects of the corrections we have implemented to tackle two systematic effects that are particularly important for our analysis: PSF anisotropy and cluster member contamination. In particular, we estimate the amplitude of any residual systematic effects as plotted in the bottom panel of Figure 2.1.

In the KSB method, the observed galaxy polarizations are corrected for PSF anisotropy using

$$e_i \rightarrow e_i - \sum_j P^{\rm sm}_{ij} p^*_j, \tag{2.5}$$

where the smear polarizability $P^{\rm sm}$ quantifies how susceptible a source is to PSF distortions and p_j is the PSF anisotropy measured using point-like sources (see e.g. Hoekstra et al., 1998).

The observed polarizations and polarizabilities are, however, biased because of noise in the images. If unaccounted for, this leads to biased cluster masses. For the shear, these corrections can be expressed in terms of a multiplicative and additive bias, μ and b:

$$\gamma_i \rightarrow (1+\mu)\gamma_i + b. \tag{2.6}$$

To ensure accurate mass estimates, H15 focused on the impact of multiplicative bias. To do so, they used image simulations with a circular PSF to calibrate the bias as a function of source SNR and size. However, the actual PSF is not round and H15, therefore, quantified the impact of an anisotropic PSF on the multiplicative bias correction. The details of these simulations, based on `galsim` (Rowe et al., 2015), can be found in section 2.2 and appendix A of H15. The galaxy properties are based on HST observations, resulting in images that match the cluster data. The PSF is modeled as a Moffat profile, which is a good representation of ground-based data. Appendix A in H15 examines the impact of PSF anisotropy and revealed that about 4 percent of this source of bias remains after correction (see their fig. A1). While the impact of this residual bias is negligible, further study revealed that it can be reduced by empirically correcting the smear polarizability for noise bias. We have increased $P^{\rm sm}$ by a factor of 1.065, such that no residual additive bias remains visible, see Figure 2.2. We also verified that this latest correction does not introduce significant trends with source characteristics. We use the difference between the ensemble lensing signal measured before and after this improvement as a (conservative) estimate of any unknown systematics affecting the shape measurement method.

The second effect we account for is the presence of cluster members in our source catalogs. Note that in this case, we have not updated the methodology from H15, but we still report it here for completeness. If we assume that cluster members are randomly oriented, as found by Sifón et al. (2015), their inclusion among our sources has the effect

of diluting the measured shear. To correct for this, we multiply $\gamma_t(R)$ by a boost factor $B(R)$ defined as a function of the projected comoving distance R:

$$B(R) = 1 + f_{\rm cont}(R)/f_{\rm obs}(R). \tag{2.7}$$

The contamination term $f_{\rm cont}$ accounts for the decrease of the ellipticity average due to the presence unsheared sources and, by comparison with blank fields, it is found to be (1) a decreasing function of distance from the cluster center and (2) negligible beyond a distance $r_{\rm max}$. An extra factor $f_{\rm obs}$ is also introduced to model the reduced background galaxy counts due to obscuration by cluster members. This factor is computed by stacking the cluster images with simulated blank fields and measuring how many simulated sources are obscured.

The functions appearing in the boost factor are written empirically as

$$\frac{1}{f_{\rm obs}(R)} = 1 + \frac{0.021}{0.14 + (R/r_{500})^2} \text{ and} \tag{2.8}$$

$$f_{\rm cont}(R) = n_0 \left(\frac{1}{R + R_c} - \frac{1}{r_{\rm max} + R_c} \right); \tag{2.9}$$

where n_0 and R_c are fitted independently for each cluster and $B(R) = 0$ for $R > r_{\rm max} \equiv 4(1+z)$ Mpc.

To quantify the amplitude of residual systematics for this second correction, we refer to H15, where a residual scatter of about 2 percent around the ensemble correction was reported.

2.3 Splashback

In this main part of the chapter, we fit the observed weak lensing signal using the spherical density profile presented in DK14. This profile is designed to reproduce the expected flattening of the density profile at large radii due to the presence of infalling material, as seen in numerical simulations.

2.3.1 Fitting procedure

The projected surface density profile $\Sigma(R)$ for a spherical lens with matter density $\rho(r)$ is:

$$\Sigma(R) = 2 \int_0^\infty dr' \, \rho \left(\sqrt{r'^2 + R^2} \right), \tag{2.10}$$

where we limit the integration range of the line of sight variable r' to $[0, 40]$ Mpc for our numerical calculations. We also verify that the chosen upper limit has no effect on our results by repeating the analysis with a wider range $[0, 80]$ Mpc. For cosmological

overdensities, this profile can be connected to the lensing signal through Eqs. 2.2 and 2.4.

In this section we use a model for $\rho(r)$ first introduced by DK14 with the following components: an Einasto profile $\rho_{\rm Ein}$ (Einasto, 1965) to model the inner dark matter halo, a transition term $f_{\rm trans}(r)$ to capture a steepening effect at the halo edge and a power-law $\rho_{\rm out}(r)$ to model the distribution of infalling material in the outer regions. The mathematical expressions are the following:

$$\rho(r) = \rho_{\rm Ein}(r) f_{\rm trans}(r) + \rho_{\rm out}(r); \tag{2.11}$$

$$\rho_{\rm Ein}(r) = \rho_{\rm s} \exp\left(-\frac{2}{\alpha}\left[\left(\frac{r}{r_{\rm s}}\right)^{\alpha} - 1\right]\right), \tag{2.12}$$

$$f_{\rm trans}(r) = \left[1 + \left(\frac{r}{r_{\rm t}}\right)^{\beta}\right]^{-\gamma/\beta}, \tag{2.13}$$

$$\rho_{\rm out} = \rho_0 \left(\frac{r}{r_0}\right)^{-s_e}. \tag{2.14}$$

In DK14 the infalling term includes an offset corresponding to the average matter density, but this is not present in our fitting function because the tangential shear in Equation (2.2) is completely insensitive to it.

In its general form, this model depends on a large number of parameters. In order to reduce its degrees of freedom we, therefore, choose to set strong priors on a few parameters. As done in Baxter et al. (2017) and Chang et al. (2018) we do not fit both ρ_0 and r_0, but choose to fix one of them, as they are degenerate. We impose Gaussian priors $\log(0.2) \pm 0.1$, $\log(6) \pm 0.2$ and $\log(4) \pm 0.2$ on the logarithms of the exponents $\log\alpha$, $\log\beta$, and $\log\gamma$, respectively. The loose prior on the Einasto shape parameter α is motivated by dark matter only simulations and its 1σ interval covers the expected scatter due to the redshift and mass distribution of our sample (Gao et al., 2008; Dutton and Macciò, 2014), while for the exponents in the transition term the stringent priors are centered on the values suggested by DK14. We also set a Gaussian prior on the truncation radius r_t, 4 ± 2, based on the same results. The location of the median is based on the r_{200m} inferred from our NFW fit and the selected standard deviation covers the expected range due to the mass distribution of our sample. Finally, based on previous measurements, we also set a minimum value of 1 for the outer slope s_e and a physically motivated minimum value of 0 for the density parameters ρ_s and ρ_0.

A rescaling of the radial coordinate with an overdensity radius (e.g. r_{200m}) is often employed when fitting the profile described above. We also attempt to rescale our coordinates with either r_{500c} or r_{200m}, but due to the uncertainties on the individual cluster profiles, no rescaling results in the splashback feature being constrained with

higher precision. Despite this, we still attempt to remove the redshift dependence of the average matter density of the Universe by using comoving coordinates.

We follow Umetsu and Diemer (2017) and do not include a miscentering term in our tangential shear model. In general, a shift in position of the cluster centres reported in Table 2.1 would cause a smoothing of the lensing profile in the central region. An estimate of the area affected by such an effect can be obtained by considering the difference between two independent estimators of the halo centre: the position of the brightest cluster galaxy or the X-ray luminosity peak. Our sample is found to be well centered (see M13) with the root mean square of the offset between the two $\sigma_{\rm off} = 33$ kpc. For the scales plotted in Figure 2.3 we therefore do not expect our data to be affected by miscentering.

A fit to input data $\gamma_t(R)$ with the covariance matrix defined in Sec. 2.2 is performed by sampling the posterior distribution of the parameters $[\rho_s, r_s, \log\alpha, r_t, \log\beta, \log\gamma, \rho_0, s_e]$ using the Markov Chain Monte Carlo ensemble sampler emcee[3] (Foreman-Mackey et al. 2013, based on Goodman and Weare 2010).

2.3.2 Interpretation

Figure 2.3 visually presents our results. The left-hand panel shows the best-fitting model to the lensing signal, while the right-hand panel shows the posterior distribution of the inferred profile. To better highlight the splashback feature we choose to focus on the dimensionless logarithmic slope $\gamma = d\log\rho/d\log r = r/\rho\ d\rho/dr$ when plotting the posterior of our model.

For both CCCP samples considered a minimum of the slope is identified. At larger distances, the results are the least interesting. In these regions, the power-law term becomes dominant and the value of the slope is set exclusively by the exponent s_e. In particular, its lower limit is artificially imposed by our prior.

What is more relevant to our study is the minimum value of the slope $\gamma(r)$ and its location, i.e. the splashback radius $r_{\rm sp}$. The 68 percent credible intervals of both quantities are indicated as shaded sections of the vertical and horizontal histograms. Our measured 99.7 percent confidence interval of $\gamma(r_{\rm sp})$ for the full sample is $[-10.9, -2.3]$, meaning that we are unable to measure a significant departure from the slope expected for an NFW profile (about -2.5). Despite this, we are still able to constrain the value of both the splashback radius and the logarithmic slope at this point, $r_{\rm sp} = 3.5^{+1.1}_{-0.7}$ Mpc and $\gamma(r_{\rm sp}) = -4.3^{+1.0}_{-1.5}$. We also highlight that the high-mass sample returns similar constraints with only half the sample size, $r_{\rm sp} = 3.5^{+1.3}_{-0.8}$ and $\gamma(r_{\rm sp}) = -3.7^{+0.9}_{-1.6}$.

As a point of reference, we also show the expected profiles from a suite of zoom-in hydrodynamical simulations of massive clusters (Hydrangea, Bahé et al., 2017). From the full Hydrangea sample, we have selected the eight most massive clusters for this comparison in order to obtain a sample with an average value of $\langle M_{200m}\rangle = 1.7\times10^{15}$

[3] https://emcee.readthedocs.io/

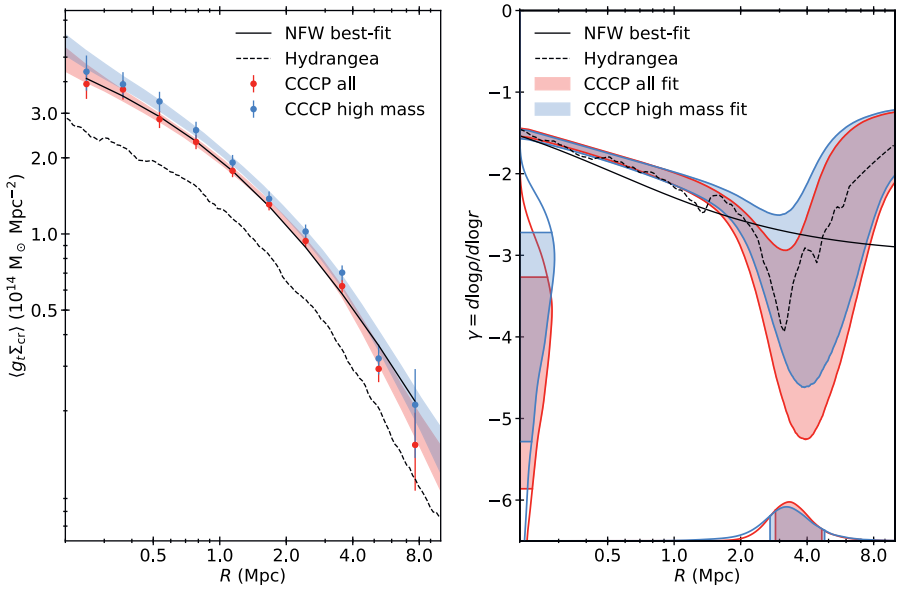

Figure 2.3: Splashback measurement. The left-hand panel shows the measured lensing signal for our full sample and a subsample of the 13 most massive clusters as a function of comoving clustercentric distance, together with the 68 percent confidence intervals from the DK14 fit. The right-hand panel shows the posterior of the three-dimensional logarithmic slope for the same model. The histograms on the horizontal axis are the distributions of the inferred position for the minimum of γ (i.e. the splashback radius $r_{\rm sp}$), while the histograms on the vertical axis are the distributions of $\gamma(r_{\rm sp})$. The solid black lines refer to the NFW fit shown in Figure 2.1, while the dashed lines correspond to predictions from hydrodynamical simulations of massive clusters (Hydrangea). The amplitude of the Hydrangea and CCCP signals are different because we match the virial mass of our observed sample at $z \gtrsim 0.2$ with simulated clusters at $z = 0$.

$M_\odot$, similar to our dataset, but evaluated at $z = 0$ instead of $z = 0.2$. Note that the amplitude of the signal plotted in Figure 2.3 is lower than the observed sample due the evolution of the average matter density of the Universe. Our slope measurements are found to be agreement with what is seen in simulations.

As done in Umetsu and Diemer (2017), we study the impact of the model parameters on the predictions for $r_{\rm sp}$ and $\gamma(r_{\rm sp})$ to verify that our dataset is informative and we are not simply sampling our model priors. Of crucial importance is the truncation radius r_t, which, in the original definition of the DK14 profile, explicitly sets the position of the splashback feature.

Similarly to Umetsu and Diemer (2017), we also find that we are unable to fully constrain this parameter. This can be seen in Figure 2.4, where we plot the posteriors of three relevant parameters for two different choices of the r_t prior: the Gaussian assumed in our main study and a flat prior in the range $[0, 20]$ Mpc. While the posterior for $\gamma(r_{\rm sp})$ (middle row) is mostly unaffected by this choice, we obtain a looser upper limit on the splashback radius (top panel) in the second case: $r_{\rm sp} = 3.9^{+2.4}_{-0.9}$. As visible in the bottom-left panel, this is due to a clear correlation with r_t.

We find no correlation between $r_{\rm sp}$ and $r_{\rm t}$ for $r_t \gtrsim 10$ Mpc. In this regime, the location of the minimum of $\gamma(r)$ is controlled by the presence of the infalling term $\rho_{in}(r) \propto r^{-s_e}$. Because the slope s_e is relatively gentle, if r_t is large enough the truncation happens in a region dominated by the infalling material and cannot be constrained. Because the truncation is expected to be visible in the transition regime, our Gaussian prior on r_t effectively forces it to a physically motivated position and, from the figure, we confirm that it does not introduce a biased posterior peak.

2.4 Conclusions

We have shown in this work that targeted weak lensing observations of massive clusters can be used to measure the splashback feature and that particular care is required when correcting for residual PSF contaminations, which should be well understood, and estimating the data covariance matrix, which should take into account the presence of additional structure along the line of sight. Using a stack of 27 massive clusters from CCCP we have fully constrained for the first time the splashback radius around massive clusters, $r_{\rm sp} = 3.6^{+1.2}_{-0.7}$, and similar precision has also been achieved with as little as 13 objects. We stress that, because of the purely gravitational nature of weak lensing, minimal assumptions are required to interpret our signal.

In the last few years, the study of the physics of accretion at the outskirts of massive dark matter halos has become observationally viable. Splashback offers a unique view into the phase-space configuration of halos, which has not yet been explored in observations. In particular, the physics behind it appears to be remarkably uncomplicated and semianalytical models of spherical collapse for cold dark matter are able to reproduce the expectations from N-body simulations (e.g. Adhikari et al., 2014; Shi, 2016).

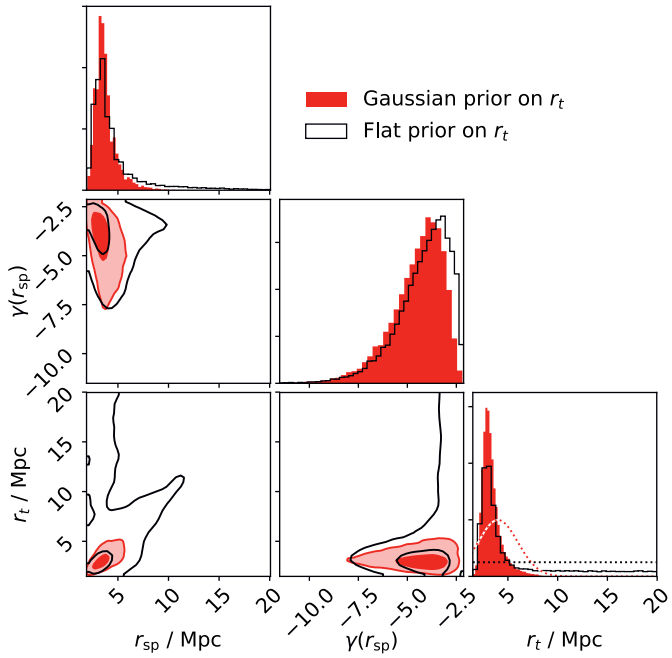

Figure 2.4: Impact of the prior on the truncation radius $r_{\rm t}$ on our results. The corner plot presents the two-dimensional and marginalized posterior distributions for the DK14 parameter r_t, the inferred splashback position $r_{\rm sp}$, and logarithmic slope $\gamma(r_{\rm sp})$. If, instead of a Gaussian prior (dashed red line), a flat prior is assumed (dashed black line), the parameter r_t has no upper bound. This translates into weaker constraints on $r_{\rm sp}$.

The fact that these results are based only on the dynamics of collapsing dark matter in an expanding Universe makes splashback a remarkable prediction of general relativity and dark matter. More generally, its connection to the growth of cosmological structures makes it a test for ΛCDM. As an example, it has also been shown recently that modifications of gravity have a significant impact on this feature (Adhikari et al., 2018). As the first results are starting to appear in the literature, we argue that splashback solicits further investigation exactly because it is a falsifiable prediction of the current paradigm.

We found that at the relevant scales a significant contribution to the lensing signal is cosmic noise. In the near future, this term can be reduced significantly with larger cluster samples. Looking further ahead, deep wide-area surveys such as *Euclid* (Laureijs et al., 2011) and LSST (LSST Science Collaboration et al., 2009) will provide unprecedented depth and survey area, and thus deliver the data required to study splashback over a wider mass and redshift range.

Appendix

2A Noise covariance matrix

For each cluster we model the noise covariance matrix for the lensing signal as the sum of two components:

$$\boldsymbol{C} = \boldsymbol{C}^{\rm stat} + \boldsymbol{C}^{\rm lss}. \tag{2.15}$$

The first is a diagonal matrix accounting for the statistical error on the weighted average of the measured ellipticities and the second quantifies the additional shear variance caused by the presence of cosmic structure between viewer and source (Hoekstra, 2003; Umetsu et al., 2011)

$$\boldsymbol{C}^{\rm lss}_{i,j} = 2\pi \int_0^\infty d\ell\ \ell P_\kappa(\ell) g(\ell,\theta_i) g(\ell,\theta_j), \tag{2.16}$$

where $P_\kappa(\ell)$ represents the projected convergence power spectrum for the multipole number ℓ. For an angular bin θ extending from θ_- to θ_+, $g(l,\theta)$ is defined using the Bessel functions of the first kind of order zero and one, J_0 and J_1:

$$\begin{aligned} g(\ell,\theta) = &\left[\frac{1-2\ln\theta_-}{\pi(\theta_+^2-\theta_-^2)}\right]\frac{\theta_- J_1(\ell\theta_-)}{\ell} - \left[\frac{1-2\ln\theta_+}{\pi(\theta_+^2-\theta_-^2)}\right]\frac{\theta_+ J_1(\ell\theta_+)}{\ell} \\ &-\frac{2}{\pi(\theta_+^2-\theta_-^2)}\int_{\theta_1}^{\theta_2} d\phi\ \phi\log\phi J_0(l\phi). \end{aligned} \tag{2.17}$$

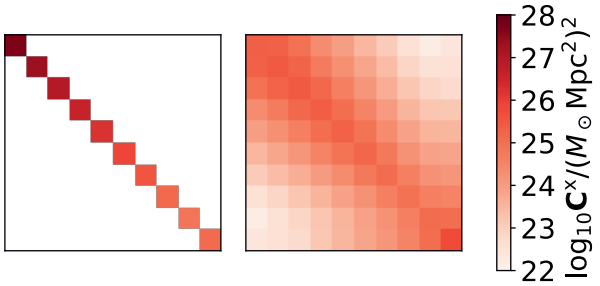

Figure 2.5: Covariance matrix. Visualization of the two components of the covariance matrix $\boldsymbol{C} = \boldsymbol{C}^{\rm stat} + \boldsymbol{C}^{\rm lss}$ for the data points plotted in Figure 2.1. The diagonal matrix (left) is the statistical error $\boldsymbol{C}^{\rm stat}$, the second one (right) is the component due to uncorrelated structure along the line of sight, $\boldsymbol{C}^{\rm lss}$. The top-left corner corresponds to the first data point.

For a given cosmology, $P_\kappa(\ell)$ can be evaluated using the Limber projection starting from a source redshift distribution and a model for the nonlinear matter power-spectrum (Kilbinger, 2015). For this work, this is done using CAMB[4] (Lewis, 2013) and HALOFIT (Takahashi et al., 2012). As an example, the resulting covariance matrices for the average signal in Fig. 1 are presented in Figure 2.5.

A third term accounting for the intrinsic variance in a particular realization of galaxy clusters should be added to the matrix in Equation (2.15). For massive clusters in the considered redshift range, this term is found to be dominated by Poissonian scatter in the number of halos contained within the correlated neighborhood (Gruen et al., 2015). We neglect this term because in similar lensing analyses (e.g. Umetsu et al., 2016; Miyatake et al., 2018) it is always found to be sub-dominant to statistical and large-scale structure noise, especially on the scales of interest for this work.

[4]https://camb.info/

Bibliography

Susmita Adhikari, Neal Dalal, and Robert T Chamberlain. Splashback in accreting dark matter halos. *Journal of Cosmology and Astroparticle Physics*, 2014(11):019–019, November 2014. ISSN 1475-7516. doi: 10.1088/1475-7516/2014/11/019.

Susmita Adhikari, Jeremy Sakstein, Bhuvnesh Jain, Neal Dalal, and Baojiu Li. Splashback in galaxy clusters as a probe of cosmic expansion and gravity. J. Cosmology Astropart. Phys., 2018(11):033, November 2018. doi: 10.1088/1475-7516/2018/11/033.

Yannick M. Bahé, David J. Barnes, Claudio Dalla Vecchia, Scott T. Kay, Simon D. M. White, Ian G. McCarthy, Joop Schaye, Richard G. Bower, Robert A. Crain, Tom Theuns, Adrian Jenkins, Sean L. McGee, Matthieu Schaller, Peter A. Thomas, and James W. Trayford. The Hydrangea simulations: galaxy formation in and around massive clusters. *Monthly Notices of the Royal Astronomical Society*, 470(4):4186–4208, October 2017. ISSN 0035-8711. doi: 10.1093/mnras/stx1403.

Eric Baxter, Chihway Chang, Bhuvnesh Jain, Susmita Adhikari, Neal Dalal, Andrey Kravtsov, Surhud More, Eduardo Rozo, Eli Rykoff, and Ravi K Sheth. The Halo Boundary of Galaxy Clusters in the SDSS. *The Astrophysical Journal*, 841(1):18, May 2017. ISSN 1538-4357. doi: 10.3847/1538-4357/aa6ff0.

Greg L. Bryan and Michael L. Norman. Statistical Properties of X-Ray Clusters: Analytic and Numerical Comparisons. *The Astrophysical Journal*, 495(1):80–99, March 1998. ISSN 0004-637X. doi: 10.1086/305262.

Philipp Busch and Simon D. M. White. Assembly bias and splashback in galaxy clusters. *Monthly Notices of the Royal Astronomical Society*, 470(4):4767–4781, October 2017. ISSN 0035-8711. doi: 10.1093/mnras/stx1584.

C. Chang, E. Baxter, B. Jain, C. Sánchez, S. Adhikari, T. N. Varga, Y. Fang, E. Rozo, E. S. Rykoff, A. Kravtsov, D. Gruen, W. Hartley, E. M. Huff, M. Jarvis, A. G. Kim, J. Prat, N. MacCrann, T. McClintock, A. Palmese, D. Rapetti, R. P. Rollins, S. Samuroff, E. Sheldon, M. A. Troxel, R. H. Wechsler, Y. Zhang, J. Zuntz, T. M. C. Abbott, F. B.

Abdalla, S. Allam, J. Annis, K. Bechtol, A. Benoit-Lévy, G. M. Bernstein, D. Brooks, E. Buckley-Geer, A. Carnero Rosell, M. Carrasco Kind, J. Carretero, C. B. D'Andrea, L. N. da Costa, C. Davis, S. Desai, H. T. Diehl, J. P. Dietrich, A. Drlica-Wagner, T. F. Eifler, B. Flaugher, P. Fosalba, J. Frieman, J. García-Bellido, E. Gaztanaga, D. W. Gerdes, R. A. Gruendl, J. Gschwend, G. Gutierrez, K. Honscheid, D. J. James, T. Jeltema, E. Krause, K. Kuehn, O. Lahav, M. Lima, M. March, J. L. Marshall, P. Martini, P. Melchior, F. Menanteau, R. Miquel, J. J. Mohr, B. Nord, R. L. C. Ogando, A. A. Plazas, E. Sanchez, V. Scarpine, R. Schindler, M. Schubnell, I. Sevilla-Noarbe, M. Smith, R. C. Smith, M. Soares-Santos, F. Sobreira, E. Suchyta, M. E. C. Swanson, G. Tarle, J. Weller, and DES Collaboration. The Splashback Feature around DES Galaxy Clusters: Galaxy Density and Weak Lensing Profiles. ApJ, 864:83, September 2018. doi: 10.3847/1538-4357/aad5e7.

A Cooray and R Sheth. Halo models of large scale structure. *Physics Reports*, 372(1): 1–129, December 2002. ISSN 03701573. doi: 10.1016/S0370-1573(02)00276-4.

DES Collaboration. Dark Energy Survey Year 1 Results: Cosmological Constraints from Galaxy Clustering and Weak Lensing. August 2017.

Benedikt Diemer and Andrey V. Kravtsov. Dependence of the outer density profiles of halos on their mass accretion rate. *The Astrophysical Journal*, 789(1):1, June 2014. ISSN 0004-637X. doi: 10.1088/0004-637X/789/1/1.

Benedikt Diemer, Surhud More, and Andrey V. Kravtsov. The pseudo-evolution of halo mass. *The Astrophysical Journal*, 766(1):25, March 2013. ISSN 0004-637X. doi: 10.1088/0004-637X/766/1/25.

Aaron A. Dutton and Andrea V. Macciò. Cold dark matter haloes in the Planck era: evolution of structural parameters for Einasto and NFW profiles. *Monthly Notices of the Royal Astronomical Society*, 441(4):3359–3374, July 2014. ISSN 1365-2966. doi: 10.1093/mnras/stu742.

J Einasto. On the Construction of a Composite Model for the Galaxy and on the Determination of the System of Galactic Parameters. *Trudy Astrofizicheskogo Instituta Alma-Ata*, 5:87–100, 1965.

James A Fillmore and Peter Goldreich. Self-similar gravitational collapse in an expanding universe. *The Astrophysical Journal*, 281:1, 1984. ISSN 0004-637X. doi: 10.1086/162070.

Daniel Foreman-Mackey, David W. Hogg, Dustin Lang, and Jonathan Goodman. emcee: The MCMC Hammer. *Publications of the Astronomical Society of the Pacific*, 125(925): 306–312, March 2013. ISSN 00046280. doi: 10.1086/670067.

Liang Gao, Julio F. Navarro, Shaun Cole, Carlos S. Frenk, Simon D. M. White, Volker Springel, Adrian Jenkins, and Angelo F. Neto. The redshift dependence of the structure of massive Λ cold dark matter haloes. *Monthly Notices of the Royal Astronomical Society*, 387(2):536–544, June 2008. ISSN 0035-8711. doi: 10.1111/j.1365-2966.2008.13277.x.

Jonathan Goodman and Jonathan Weare. Ensemble samplers with affine invariance. *Communications in Applied Mathematics and Computational Science*, 5(1):65–80, January 2010. ISSN 2157-5452. doi: 10.2140/camcos.2010.5.65.

D. Gruen, S. Seitz, M. R. Becker, O. Friedrich, and A. Mana. Cosmic variance of the galaxy cluster weak lensing signal. *Monthly Notices of the Royal Astronomical Society*, 449(4):4264–4276, April 2015. ISSN 0035-8711. doi: 10.1093/mnras/stv532.

James E. Gunn and J. Richard III Gott. On the Infall of Matter Into Clusters of Galaxies and Some Effects on Their Evolution. *The Astrophysical Journal*, 176:1, August 1972. ISSN 0004-637X. doi: 10.1086/151605.

H. Hoekstra, M. Franx, and K. Kuijken. Hubble Space Telescope Weak-Lensing Study of the z =0.83 Cluster MS 1054-03. *The Astrophysical Journal*, 532(1):88–108, March 2000. ISSN 0004-637X. doi: 10.1086/308556.

Henk Hoekstra. How well can we determine cluster mass profiles from weak lensing? *Monthly Notices of the Royal Astronomical Society*, 339(4):1155–1162, March 2003. ISSN 0035-8711. doi: 10.1046/j.1365-8711.2003.06264.x.

Henk Hoekstra, Marijn Franx, Konrad Kuijken, and Gordon Squires. Weak Lensing Analysis of Cl 1358+62 Using Hubble Space Telescope Observations. *The Astrophysical Journal*, 504(2):636–660, September 1998. ISSN 0004-637X. doi: 10.1086/306102.

Henk Hoekstra, Andisheh Mahdavi, Arif Babul, and Chris Bildfell. The Canadian Cluster Comparison Project: weak lensing masses and SZ scaling relations. *Monthly Notices of the Royal Astronomical Society*, 427(2):1298–1311, December 2012. ISSN 00358711. doi: 10.1111/j.1365-2966.2012.22072.x.

Henk Hoekstra, Matthias Bartelmann, Håkon Dahle, Holger Israel, Marceau Limousin, and Massimo Meneghetti. Masses of Galaxy Clusters from Gravitational Lensing. *Space Science Reviews*, 177(1-4):75–118, August 2013. ISSN 0038-6308. doi: 10.1007/s11214-013-9978-5.

Henk Hoekstra, Ricardo Herbonnet, Adam Muzzin, Arif Babul, Andisheh Mahdavi, Massimo Viola, and Marcello Cacciato. The Canadian Cluster Comparison Project: detailed study of systematics and updated weak lensing masses. *Monthly Notices of the Royal Astronomical Society*, 449(1):685–714, May 2015. ISSN 1365-2966. doi: 10.1093/mnras/stv275.

Nick Kaiser, Gordon Squires, and Tom Broadhurst. A Method for Weak Lensing Observations. *The Astrophysical Journal*, 449:460, August 1995. ISSN 0004-637X. doi: 10.1086/176071.

KiDS collaboration. The third data release of the Kilo-Degree Survey and associated data products. *Astronomy & Astrophysics*, 604:A134, August 2017. ISSN 0004-6361. doi: 10.1051/0004-6361/201730747.

Martin Kilbinger. Cosmology with cosmic shear observations: a review. *Reports on Progress in Physics*, 78(8):086901, July 2015. ISSN 0034-4885. doi: 10.1088/0034-4885/78/8/086901.

C. Laigle, H. J. McCracken, O. Ilbert, B. C. Hsieh, I. Davidzon, P. Capak, G. Hasinger, J. D. Silverman, C. Pichon, J. Coupon, H. Aussel, D. Le Borgne, K. Caputi, P. Cassata, Y.-Y. Chang, F. Civano, J. Dunlop, J. Fynbo, J. S. Kartaltepe, A. Koekemoer, O. Le Fèvre, E. Le Floc'h, A. Leauthaud, S. Lilly, L. Lin, S. Marchesi, B. Milvang-Jensen, M. Salvato, D. B. Sanders, N. Scoville, V. Smolcic, M. Stockmann, Y. Taniguchi, L. Tasca, S. Toft, Mattia Vaccari, and J. Zabl. The cosmos2015 catalog: Exploring the $1 < z < 6$ universe with half a million galaxies. *The Astrophysical Journal Supplement Series*, 224(2):24, June 2016. ISSN 1538-4365. doi: 10.3847/0067-0049/224/2/24.

R. Laureijs, J. Amiaux, S. Arduini, J. . Augueres, J. Brinchmann, R. Cole, M. Cropper, C. Dabin, L. Duvet, A. Ealet, and et al. Euclid Definition Study Report. *ArXiv e-prints*, October 2011.

Antony Lewis. Efficient sampling of fast and slow cosmological parameters. *Physical Review D*, 87(10):103529, May 2013. ISSN 1550-7998. doi: 10.1103/PhysRevD.87.103529.

LSST Science Collaboration, P. A. Abell, J. Allison, S. F. Anderson, J. R. Andrew, J. R. P. Angel, L. Armus, D. Arnett, S. J. Asztalos, T. S. Axelrod, and et al. LSST Science Book, Version 2.0. *ArXiv e-prints*, December 2009.

G. A. Luppino and Nick Kaiser. Detection of Weak Lensing by a Cluster of Galaxies at z = 0.83. *The Astrophysical Journal*, 475(1):20–28, January 1997. ISSN 0004-637X. doi: 10.1086/303508.

Andisheh Mahdavi, Henk Hoekstra, Arif Babul, Chris Bildfell, Tesla Jeltema, and J. Patrick Henry. JOINT ANALYSIS OF CLUSTER OBSERVATIONS. II. CHANDRA / XMM-NEWTON X-RAY AND WEAK LENSING SCALING RELATIONS FOR A SAMPLE OF 50 RICH CLUSTERS OF GALAXIES. *The Astrophysical Journal*, 767(2):116, April 2013. ISSN 0004-637X. doi: 10.1088/0004-637X/767/2/116.

Hironao Miyatake, Surhud More, Masahiro Takada, David N. Spergel, Rachel Mandelbaum, Eli S. Rykoff, and Eduardo Rozo. Evidence of Halo Assembly Bias in Massive

Clusters. *Physical Review Letters*, 116(4):041301, January 2016. ISSN 0031-9007. doi: 10.1103/PhysRevLett.116.041301.

Hironao Miyatake, Nicholas Battaglia, Matt Hilton, Elinor Medezinski, Atsushi J Nishizawa, Surhud More, Simone Aiola, Neta Bahcall, J Richard Bond, Erminia Calabrese, Steve K Choi, Mark J Devlin, Joanna Dunkley, Rolando Dunner, Brittany Fuzia, Patricio Gallardo, Megan Gralla, Matthew Hasselfield, Mark Halpern, Chiaki Hikage, J. Colin Hill, Adam D. Hincks, Renée Hložek, Kevin Huffenberger, John P. Hughes, Brian Koopman, Arthur Kosowsky, Thibaut Louis, Mathew S. Madhavacheril, Jeff McMahon, Rachel Mandelbaum, Tobias A. Marriage, Loïc Maurin, Satoshi Miyazaki, Kavilan Moodley, Ryoma Murata, Sigurd Naess, Laura Newburgh, Michael D. Niemack, Takahiro Nishimichi, Nobuhiro Okabe, Masamune Oguri, Ken Osato, Lyman Page, Bruce Partridge, Naomi Robertson, Neelima Sehgal, Masato Shirasaki, Jonathan Sievers, Cristóbal Sifón, Sara Simon, Blake Sherwin, David N Spergel, Suzanne T Staggs, George Stein, Masahiro Takada, Hy Trac, Keiichi Umetsu, Alex van Engelen, and Edward J Wollack. Weak-Lensing Mass Calibration of ACTPol Sunyaev-Zel'dovich Clusters with the Hyper Suprime-Cam Survey. April 2018.

Surhud More, Benedikt Diemer, and Andrey V. Kravtsov. The splashback radius as a physical halo boundary and the growth of halo mass. *The Astrophysical Journal*, 810 (1):36, August 2015. ISSN 1538-4357. doi: 10.1088/0004-637X/810/1/36.

Surhud More, Hironao Miyatake, Masahiro Takada, Benedikt Diemer, Andrey V. Kravtsov, Neal K. Dalal, Anupreeta More, Ryoma Murata, Rachel Mandelbaum, Eduardo Rozo, Eli S. Rykoff, Masamune Oguri, and David N. Spergel. Detection of the splashback radius and halo assembly bias of massive galaxy clusters. *The Astrophysical Journal*, 825(1):39, June 2016. ISSN 1538-4357. doi: 10.3847/0004-637X/825/1/39.

Julio F. Navarro, Carlos S. Frenk, and Simon D. M. White. A Universal Density Profile from Hierarchical Clustering. *The Astrophysical Journal*, 490(2):493–508, December 1997. ISSN 0004-637X. doi: 10.1086/304888.

Planck Collaboration. Planck 2015 results. *Astronomy & Astrophysics*, 594:A13, October 2016. ISSN 0004-6361. doi: 10.1051/0004-6361/201525830.

B. T. P. Rowe, M. Jarvis, R. Mandelbaum, G. M. Bernstein, J. Bosch, M. Simet, J. E. Meyers, T. Kacprzak, R. Nakajima, J. Zuntz, H. Miyatake, J. P. Dietrich, R. Armstrong, P. Melchior, and M. S. S. Gill. GALSIM: The modular galaxy image simulation toolkit. *Astronomy and Computing*, 10:121–150, April 2015. doi: 10.1016/j.ascom.2015.02.002.

E. S. Rykoff, E. Rozo, M. T. Busha, C. E. Cunha, A. Finoguenov, A. Evrard, J. Hao, B. P. Koester, A. Leauthaud, B. Nord, M. Pierre, R. Reddick, T. Sadibekova, E. S. Sheldon, and R. H. Wechsler. redmapper. i. algorithm and sdss dr8 catalog. *The Astrophysical Journal*, 785(2):104, April 2014. ISSN 0004-637X. doi: 10.1088/0004-637X/785/2/104.

Xun Shi. The outer profile of dark matter haloes: an analytical approach. *Monthly Notices of the Royal Astronomical Society*, 459(4):3711–3720, July 2016. ISSN 0035-8711. doi: 10.1093/mnras/stw925.

Cristóbal Sifón, Henk Hoekstra, Marcello Cacciato, Massimo Viola, Fabian Köhlinger, Remco F. J. van der Burg, David J. Sand, and Melissa L. Graham. Constraints on the alignment of galaxies in galaxy clusters from ˜14000 spectroscopic members. *Astronomy & Astrophysics*, 575:A48, March 2015. ISSN 0004-6361. doi: 10.1051/0004-6361/201424435.

Ryuichi Takahashi, Masanori Sato, Takahiro Nishimichi, Atsushi Taruya, and Masamune Oguri. Revising the halofit model for the nonlinear matter power spectrum. *The Astrophysical Journal*, 761(2):152, December 2012. ISSN 0004-637X. doi: 10.1088/0004-637X/761/2/152.

Keiichi Umetsu and Benedikt Diemer. Lensing Constraints on the Mass Profile Shape and the Splashback Radius of Galaxy Clusters. *The Astrophysical Journal*, 836(2):231, April 2017. ISSN 1538-4357. doi: 10.3847/1538-4357/aa5c90.

Keiichi Umetsu, Tom Broadhurst, Adi Zitrin, Elinor Medezinski, Dan Coe, and Marc Postman. A precise cluster mass profile averaged from the highest-quality lensing data. *The Astrophysical Journal*, 738(1):41, September 2011. ISSN 0004-637X. doi: 10.1088/0004-637X/738/1/41.

Keiichi Umetsu, Adi Zitrin, Daniel Gruen, Julian Merten, Megan Donahue, and Marc Postman. Clash: Joint analysis of strong-lensing, weak-lensing shear, and magnification data for 20 galaxy clusters. *The Astrophysical Journal*, 821(2):116, April 2016. ISSN 1538-4357. doi: 10.3847/0004-637X/821/2/116.

Ying Zu, Rachel Mandelbaum, Melanie Simet, Eduardo Rozo, and Eli S. Rykoff. On the level of cluster assembly bias in SDSS. *Monthly Notices of the Royal Astronomical Society*, 470(1):551–560, September 2017. ISSN 0035-8711. doi: 10.1093/mnras/stx1264.